JACS
JOURNAL OF THE AMERICAN CHEMICAL SOCIETY
Article
Cite This: J. Am. Chem. Soc. XXXX, XXX, XXX−XXX
pubs.acs.org/JACS

Synthetic Control over Quantum Well Width Distribution and Carrier Migration in Low-Dimensional Perovskite Photovoltaics

Andrew H. Proppe,[†,‡] Rafael Quintero-Bermudez,[‡] Hairen Tan,[‡] Oleksandr Voznyy,[‡] Shana O. Kelley,[†,§] and Edward H. Sargent*[,‡]

[†]Department of Chemistry, University of Toronto, 80 St. George Street, Toronto, Ontario, Canada, M5S 3G4

[‡]The Edward S. Rogers Department of Electrical and Computer Engineering, University of Toronto, 10 King's College Road, Toronto, Ontario, Canada, M5S 3G4

[§]Department of Pharmaceutical Sciences, Leslie Dan Faculty of Pharmacy, University of Toronto, Toronto, Ontario, Canada, M5S 3M2

Supporting Information

ABSTRACT: Metal halide perovskites have achieved photovoltaic efficiencies exceeding 22%, but their widespread use is hindered by their instability in the presence of water and oxygen. To bolster stability, researchers have developed low-dimensional perovskites wherein bulky organic ligands terminate the perovskite lattice, forming quantum wells (QWs) that are protected by the organic layers. In thin films, the width of these QWs exhibits a distribution that results in a spread of bandgaps in the material arising due to varying degrees of quantum confinement across the population. Means to achieve refined control over this QW width distribution, and to examine and understand its influence on photovoltaic performance, are therefore of intense interest. Here we show that moving to the ligand allylammonium enables a narrower distribution of QW widths, creating a flattened energy landscape that leads to ×1.4 and ×1.9 longer diffusion lengths for electrons and holes, respectively. We attribute this to reduced ultrafast shallow hole trapping that originates from the most strongly confined QWs. We observe an increased PCE of 14.4% for allylammonium-based perovskite QW photovoltaics, compared to 11−12% PCEs obtained for analogous devices using phenethylammonium and butylammonium ligands. We then optimize the devices using mixed-cation strategies, achieving 16.5% PCE for allylammonium devices. The devices retain 90% of their initial PCEs after >650 h when stored under ambient atmospheric conditions.

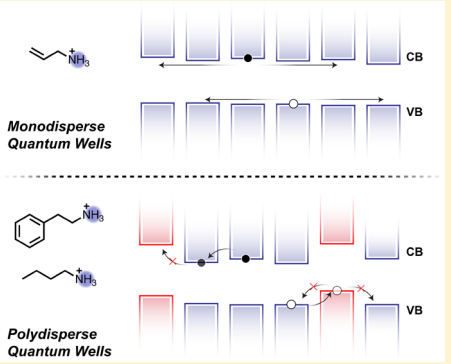

INTRODUCTION

Organic−inorganic metal halide perovskites are solution-processed semiconductors with remarkable photophysical and optoelectronic properties. Their composition is readily tuned via precursor stoichiometry during solution-phase processing, enabling perovskite materials with long carrier diffusion lengths and balanced mobilities,[1,2] low defect densities,[3,4] and tunable bandgaps,[5,6] giving rise to efficient light-harvesting and light-emitting devices[7] based on these materials.

In light of their potential for scalable and inexpensive processing, these materials hold promise for thin film solar cells in view of their impressive power conversion efficiencies (PCEs) that have now exceeded 22%. The stability of perovskite active layers, especially in the presence of moisture which can travel through low-cost flexible encapsulants, remains a priority area for further research and development.[6,8]

Low-dimensional perovskites consist of perovskite quantum wells (QWs) whose lattice is terminated along one axis using bulky organic ligands such as butylammonium ($C_4H_9NH_3^+$) or phenethylammonium ($C_8H_9NH_3^+$) (Figure 1a). This results in quantum confinement within the resultant perovskite domains: the energy levels, as in conventional QWs, vary with the thickness of the nanoplatelets, and hence with the number of monolayers, n, that reside between the bulk-terminating larger ligands. These outer ligands form bilayer interfaces due to van der Waals interactions, creating a stable barrier that protects the perovskite lattice against degradation (Figure 1b). Previous works have proven that the mixed perovskite QWs are more resistant to moisture and led to better device stability than their 3D counterparts.[8−13]

The QW width in solution-cast thin films is determined by the ratio of ligand molecules to perovskite A-site cations (typically methylammonium (MA), formamidinium (FA), or cesium (Cs)) in the precursor solution. Higher ratios of ligand-to-A-site cation result in lower n values. Due to thermodynamic mixing and the variable formation energy of the QWs, a mixture of QWs with varying widths is created, centered around an n (henceforth referred to as $\langle n \rangle$, the average QW width).[14,15] Lower $\langle n \rangle$ values confer higher stability but lower efficiencies,

Received: November 28, 2017
Published: February 3, 2018

DOI: 10.1021/jacs.7b12551
J. Am. Chem. Soc. XXXX, XXX, XXX−XXX

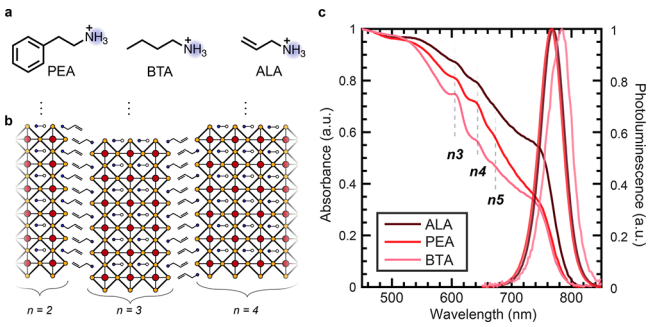

Figure 1. Organic ligand molecules, low-dimensional perovskite quantum wells, and absorption and emission spectra. (a) Molecules used as ligands in this work: allylammonium (ALA), phenethylammonium (PEA), and butylammonium (BTA). (b) Schematic illustration of low-dimensional perovskite quantum wells, with *n*2, *n*3, and *n*4 wells depicted here. (c) Normalized absorption and emission spectra for $\langle n \rangle$ = 10 films using the three different ligands. Excitonic peaks for quantum wells *n*3, *n*4, and *n*5 are identified.

resulting in a compromise between enhanced device lifetime and device performance by tuning $\langle n \rangle$.[8] This has been speculated to be due to the insulating nature of the molecular interfaces between perovskite domains.[8,10,14]

However, transient absorption spectroscopic studies have shown that both electrons and holes are able to transfer between perovskite QWs on a time scale of several picoseconds.[15−17] This indicates that, while overall carrier mobility is slowed, the molecular barrier separating the perovskite QWs does not fully block charge transfer. The slower charge transfer between perovskite QWs may not be the only, or even the principal, cause of lower device efficiency.[8,10]

We sought to determine properties of the low-$\langle n \rangle$ mixed Q2D perovskite thin films that could lead to reduced overall photovoltaic performance and to utilize the resultant insights to address these limitations. QW polydispersity and the resultant nonflat energy landscape is expected to degrade photovoltaic material performance: carriers will funnel down into QWs with the lowest energy bands where, surrounded by a higher-bandgap environment, they may fail to be extracted to the contacts.

RESULTS AND DISCUSSION

We began our investigations with a study of how the organic ligand influences QW width distribution. The composition of the films studied here follows the formula $(L)_2(MA)_{n-1}Pb_nI_{3n-1}$, where L is the ligand molecule allylammonium (ALA), phenethylammonium (PEA), or butylammonium (BTA). We select $\langle n \rangle$ = 10, since it is known to exhibit PCEs in the range 10−12% and maintain ∼90% of this efficiency after 1000 h of aging,[8] giving an opportunity to address and possibly improve the relatively low efficiency in a reasonably stable material. Figure 1c shows the absorption and photoluminescence (PL) spectra of the $\langle n \rangle$ = 10 films for the three different ligands. The absorption spectra are dominated by the continuum transitions of the higher-*n* QWs, but excitonic peaks for lower-*n* QWs are observable. From the absorption onset and band-edge transitions, it is seen that ALA induces the formation of higher-*n* QWs, and exhibits smaller peaks for the lower-*n* QWs. The emission spectra for the three ligands are all qualitatively similar, with only the BTA film having a slightly red-shifted PL peak. This would indicate the formation of more 3D perovskite domains in the material, which would have the smallest bandgap and act as a recombination center.[8,15,17]

Ultrafast transient absorption (TA) spectroscopy probes the presence of lower-*n* QWs, since the excitonic resonances are more easily resolved at early delay times without being

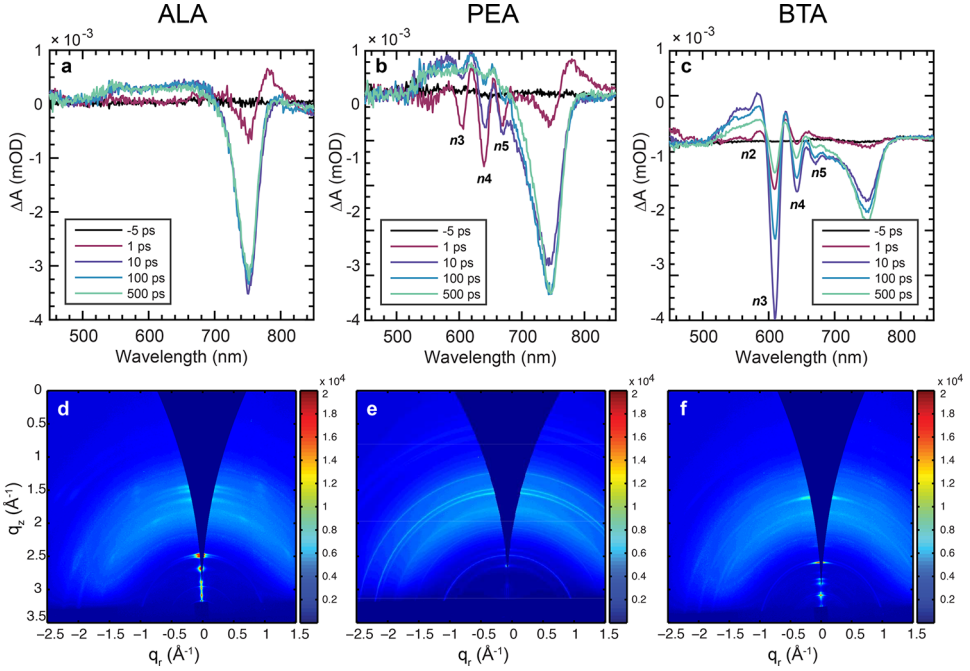

Figure 2. Ligand dependence of QW width distribution and ordering. (a−c) TA spectra at various delay times for $\langle n \rangle$ = 10 films of ALA, PEA, and BTA, respectively. The films were photoexcited at 400 nm in order to excite all possible QWs present. Lower-*n* QWs are identified according to literature references. (d−f) GIWAXS images for $\langle n \rangle$ = 3 films of ALA, PEA, and BTA, respectively. Details of GIWAXS measurements, and data for $\langle n \rangle$ = 5 and $\langle n \rangle$ = 10 films, can be found in the Supporting Information.

DOI: 10.1021/jacs.7b12551
J. Am. Chem. Soc. XXXX, XXX, XXX−XXX

obscured by continuum transitions. Figure 2a–c shows the TA spectra at various delay times for the $\langle n \rangle$ = 10 ALA, PEA, and BTA films. Negative features correspond to bleached excitonic transitions in the QWs, whereas positive features are caused by blue-shifting of the exciton peak due to hot carriers and many-body effects present at early delay times (0–5 ps).[18] The ALA film features one main bleach peak at ~750 nm, and vanishingly small amplitudes for lower-n QWs. This is in sharp contrast to the PEA and BTA films, which show peaks for QWs with n as low as 2 and 3 in the case of BTA and PEA, respectively. We fit the main exciton bleach (between ~710 and 750 nm) for the three ligands (Figure S1), and find the fwhm to be ~200 meV narrower for ALA compared to the two other ligands, showing that, within this inhomogeneously broadened peak, the distribution of QWs (e.g., n = 6–10) is narrowest for ALA. The same relationship between the ligands and the degree of polydispersity is also found in films of $\langle n \rangle$ = 3 (Figure S2).

To assess whether the choice of ligand and QW polydispersity influences crystallinity and ordering of the QWs, we carried out Grazing-Incidence Wide-Angle X-Ray Scattering (GIWAXS) measurements on films of $\langle n \rangle$ = 3, 5, and 10 using the three different ligands. We show GIWAXS diffraction patterns for the $\langle n \rangle$ = 3 films here (Figure 2d–f), since these contain more low-n QWs and exhibit brighter diffraction peaks compared to $\langle n \rangle$ = 5 and $\langle n \rangle$ = 10 films (Figure S3). It is possible to identify the morphological composition and orientation of the low-dimensional perovskite films with various ligands. Highly textured spots below 1 Å^{-1} along q_{xy} = 0 in ALA and BTA films point to the formation of low-n QWs with a high degree of spatial coherence and equally high degree of orientation with ligand bilayers parallel to the substrate. Furthermore, these films (particularly the ALA film) exhibit highly patterned spots for q > 1 Å^{-1}, evidencing a high degree of orientation of the perovskite unit cell (see Figure S4 for slices along q_z at q_{xy} = 0 for the three GIWAXS images). This observation points to a high degree of order even among larger-n QWs. This trend is decreased in the BTA film along with a concurrent rise in the intensity of the isotropic ring exhibited by disordered crystallites. The PEA film, on the other hand, exhibits weak low-n QW diffraction peaks and broad isotropic rings for q > 1 Å^{-1}, suggesting a greater disorder of the crystallites.

To understand how the QW polydispersity and presence of lower-n QWs in an otherwise homogeneous QW mix may affect transport, we use ultrafast TA to examine the carrier dynamics in highly polydisperse PEA films. $\langle n \rangle$ = 3 is again chosen to create a larger distribution of different QWs with more distinguishable excitonic resonances, such that it is easier to observe electron and hole transfer between them, and PEA is selected as the ligand, since the energy transfer rates can be compared with previous reports for this exact system.[15] Figure 3a shows the evolution of the various exciton bleaching peaks following photoexcitation at the n4 resonance (640 nm), where the hole, electron, and exciton transfer are highlighted by the dashed rectangles. Peaks at n2, n3, n5, and the mixture of n6+ begin to grow in within the first tens of picoseconds before the overall spectrum begins to decay due to recombination. Fits to the carrier dynamics are obtained with global analysis (using Glotaran,[19] see the Supporting Information). The three lifetimes used in the fitting are 9, 138, and 4300 ps. The 9 ps component accounts for ultrafast charge transfer, as can be seen from the curves in Figure 3b (rise times at 610, 666, and 700 nm, corresponding to excitonic bleach of n3, n5, and n6,

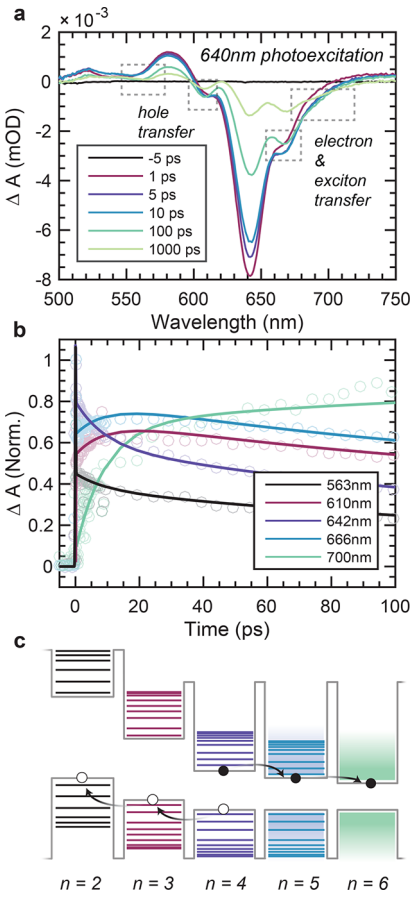

Figure 3. Ultrafast dynamics and hole trapping into low-n QWs. (a) TA spectral traces at various delay times for an $\langle n \rangle$ = 3 PEA film. Charge transfer events are highlighted in dashed gray boxes. (b) Kinetic traces and fits from global analysis at various wavelengths from 563 to 700 nm, corresponding to n2, n3, n4, n5, and n6+, respectively. (c) Schematic of the band structure for mixed low-n perovskite QWs. After photoexcitation and exciton dissociation, electrons will transfer from low- to high-n QWs, while the opposite occurs for holes owing to the type II band alignment.

respectively), whereas the other fast component is attributed to slower transport throughout the film to eventually reach the highest and lowest n QWs. The long ~4 ns component is attributed to recombination (see Figure S5 for decay associated spectra for these lifetimes and fit residuals). Transfer from low- to high-n QWs is due to exciton and electron transfer, whereas high- to low-n transfer results from hole migration. This is consistent with the band structure of mixed Q2D perovskites (Figure 3c) that has been previously determined using UPS on films[15] and single crystals,[11] as well as inferred from TA experiments.[16] Extrapolating the results from $\langle n \rangle$ = 3 PEA films, we predict that this picosecond hole transfer from high to low n would cause the lower-n QWs to act as shallow traps for holes in the device relevant $\langle n \rangle$ = 10 films.

We sought to determine if the hole-trapping low-n QWs (n = 3–6) that are more abundant in the $\langle n \rangle$ = 10 PEA- and BTA-based films would be detrimental to carrier transport. PL quenching methods have been used to study transport properties (lifetimes, diffusion lengths, and mobilities) in quantum dot solids and in bulk perovskite thin films.[2,20] We follow the formalism of Tisdale et al.,[21] which expands upon the 1D PL quenching method to determine diffusion lengths in thin films, and use the same quencher materials as in previously

DOI: 10.1021/jacs.7b12551
J. Am. Chem. Soc. XXXX, XXX, XXX–XXX

Table 1. Transport Characteristics for $\langle n \rangle$ = 10 Films from Photoluminescence Quenching Experiments

ligand	τ_{PMMA} (ns)	τ_{PCBM} (ns)	τ_{Spiro} (ns)	d (nm)	L_D (nm), e^-	L_D (nm), h^+	μ ($cm^2\ V^{-1}\ s^{-1}$), e^-
ALA	90.5	8.9	13.5	226 ± 5	633 ± 14	507 ± 11	1.1×10^0
PEA	47.9	10.7	24.7	246 ± 12	442 ± 22	266 ± 13	5.7×10^{-1}
BTA	25.3	11.9	36.7	195 ± 2	224 ± 2	76 ± 1	8.9×10^{-2}

reported quenching experiments for perovskites.[2,20] Analytical solutions to the 1D diffusion equation and some approximations lead to the following expression of the carrier diffusion length, L_D,

$$L_D \approx \frac{2d}{\pi}\sqrt{2\left(\frac{\tau}{\tau_{quench}} - 1\right)}$$

which relies only on the film thickness (d), carrier lifetime, and quenched lifetimes for electrons and holes in order to estimate the diffusion length. Small variations in thickness determine the error in estimates of L_D and other transport parameters. Figure S6 shows the fitted transient PL data for the three different films with and without the quencher layers. L_D for electrons and holes in each film and the parameters used for its calculation are shown in Table 1. Mobilities are calculated using the diffusion length equation and Einstein relation:

$$L_D = \sqrt{D\tau}$$

$$D = \mu kT/q$$

The ALA-based films have the highest L_D and μ, longest lifetimes, and most balanced transport out of the three different ligands. PEA has comparatively large L_D for electrons but is significantly limited by hole diffusion, whereas the BTA films exhibit low lifetimes and relatively poor L_D for both carriers. Again in the case of BTA, the hole diffusion length is much lower than that of the electron. These findings corroborate our ultrafast TA results, and support the notion that the presence of lower-n QWs in the $\langle n \rangle$ = 10 films for PEA and BTA should lead to shallow trapping of holes. The PL quenching studies indicate that ALA-based films benefit greatly from the lack of lower-n QWs in these materials, and also suggest that the flattened energy landscape of the more monodisperse QW width distribution assists transport, since the electron mobility of ALA is greater than both BTA and PEA. This is analogous to the influence of bandgap polydispersity on transport and photovoltaic efficiency in quantum dot solids,[22,23] where a flatter energy landscape and reduced number of shallow traps increases carrier mobility.

To examine whether the superior transport properties of ALA films were due to faster charge transfer (as a result of reduced ligand length), we performed TA experiments on mixed low-n films and monitored the lowest energy bleach peak for funneling of carriers (Figure S8). Most notably, ALA and BTA have similar transfer rates despite their different lengths. We also point out that any significantly enhanced electronic coupling from shorter ligands should result in a red-shift of the exciton peaks (as demonstrated in low-dimensional perovskites by Soe et al. using guanidinium as a ligand),[24] yet we do not observe such a red-shift here. We conclude that the small difference in ligand length between ALA, BTA, and PEA is not responsible for the longer diffusion lengths and higher mobilities in ALA films.

Anticipating that longer, balanced L_D for electrons and holes should lead to increased photovoltaic efficiency, we fabricated solar cells out of the $\langle n \rangle$ = 10 films for each ligand. J–V curves measured for devices with the three different ligands are shown in Figure 4, and their characteristics are listed in Table 2. Out of

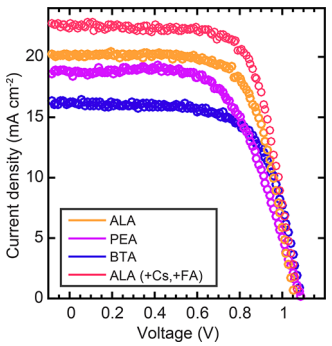

Figure 4. J–V curves for ALA, PEA, BTA, and mixed cation ALA devices. Forward bias to short-circuit current scans are shown for the various ligand-based $\langle n \rangle$ = 10 devices.

Table 2. Photovoltaic Characteristics for the $\langle n \rangle$ = 10 Devices[a]

ligand	PCE (%)	V_{OC} (V)	J_{SC} (mA cm^{-2})	FF (%)
ALA	14.4 (±0.4)	1.05	20.1	68
PEA	12.1 (±0.5)	1.08	18.4	61
BTA	11.5 (±0.4)	1.08	16.2	66
ALA (+Cs, +FA)	16.5 (±0.39)	1.07	22.6	68

[a]Characteristics are shown for the best devices for each ligand, with uncertainty in PCE derived from multiple devices.

the three different ligands, the ALA-based films show the highest power conversion efficiency (PCE) of 14.4% compared to 12.1% and 11.5% for the PEA and BTA films, respectively. While the PEA and BTA devices both possess V_{OC} similar to ALA, they are limited by the fill factor (FF) in the case of PEA and the photocurrent (J_{SC}) in the case of BTA. We note that the PCE obtained for PEA, and its stability over time when stored under ambient conditions, is very close to that previously reported for nearly identical devices (see ref 8).

Owing to the aforementioned performance–stability compromise that follows from the choice of $\langle n \rangle$, it is important to ensure that the augmented performance of ALA-based films does not arise simply due to these films having a higher $\langle n \rangle$ QW distribution after being cast into a film (e.g., if $\langle n \rangle$ = 10 was designated in solution, but a distribution closer to $\langle n \rangle$ = 20 or 30 actually formed in film due to incomplete ligand incorporation, or the varying solubility between ligands). We rule this out, since the TA peak maximum for the $\langle n \rangle$ = 10 films is roughly the same (~750 nm) for all three ligands, indicating that the mixed QWs exhibit a similar degree of confinement and therefore similar $\langle n \rangle$. We also determined the ligand-to-methylammonium (L:MA) ratios in the films by redissolving them in d^6-DMSO and then integrating the relevant peaks in ^{1}H NMR spectra. The L:MA ratios were found to be 0.32:1 ($\langle n \rangle$ = 7), 0:32:1 ($\langle n \rangle$ = 7), and 0.26:1 ($\langle n \rangle$ = 9) for ALA, PEA,

DOI: 10.1021/jacs.7b12551
J. Am. Chem. Soc. XXXX, XXX, XXX–XXX

and BTA, respectively (Figures S9–S12). This indicates that the ⟨n⟩ distribution for ALA is not artificially higher than the other ligands. Additionally, the photovoltaic devices have very similar stabilities when stored under ambient conditions, retaining roughly more than 90% of their initial PCEs after 500 h (Figure S13). If the ⟨n⟩ distribution for the ALA films were higher, the increase in performance would be accompanied by a decrease in stability.[8] We thus conclude that the ALA devices' superior performance is derived from the reduced number of lower-n QWs in these films. We also reaffirm the assessment that the lower-n QWs in PEA and BTA films act as shallow traps rather than deep traps, since such an abundance of deep traps would be expected to lead to much worse device performances.

We speculate that the higher n distribution in ALA films compared to PEA and BTA results from the differences in intermolecular bonding at the QW interfaces. The formation energies for various n value QWs using PEA have been calculated using density functional theory (DFT), and it was determined that lower-n QWs have higher formation energies due to the van der Waals and π-stacking interactions between the PEA moieties, favoring the initial formation of low-n QWs regardless of precursor stoichiometry in solution.[8] BTA molecules also have similar van der Waals interactions to stabilize the interfaces between QWs. Since ALA has only the single C═C bond to promote intermolecular interactions between QWs, we suspect that this lowers the formation energy for lower-n QWs, and thus allows for a distribution of QWs that is closer to the originally designated ratio in solution. This would suggest that the loss in formation energy would make these films more unstable and susceptible to degradation; however, our device aging studies indicate that this is not the case. A full understanding of the mechanism that links the choice of ligand with the QW n distribution is an important future direction for this field.

The composition of all of the films studied thus far follows the formula $(L)_2(MA)_{n-1}Pb_nI_{3n-1}$, i.e. iodine as the halide and MA as the A-site cations. Numerous reports indicate that perovskites with mixed halide (I/Br) and mixed cation (MA, FA, and Cs) compositions achieve higher PCEs.[6,25−27] We fabricated ⟨n⟩ = 10 perovskite devices using a mixed halide (85:15 I:Br) and mixed cation composition (0.14:0.81:0.05 MA:FA:Cs) reported to give efficiencies over 21% in 3D perovskites,[25] using the formula $ALA_2(MA_{0.14}FA_{0.81}Cs_{0.05})_9Pb_{10}(I_{0.85}Br_{0.15})_{29}$. Device performance and hysteresis depended heavily on the halides and solvents used in the precursor solution. In particular, precursor solutions containing dimethylformamide as the primary solvent resulted in much lower performance than a 1:1 mixture of dimethyl sulfoxide and γ-butyrolactone, and using a ratio of 0.15:0.85 Br to I also lowered the overall device performance (Figures S14 and S15). However, when Br is removed from this mixture but the mixed cation composition (0.81:0.14:0.05 for FA:MA:Cs) is retained, device performances up to 16.5% could be obtained via an increase in J_{SC} compared to the pure-MA devices (Figure 4), with a similar degree of hysteresis (Figure S16). These results, along with more recent reports of mixed cation perovskite QW photovoltaics,[6,9] indicate the potential of these lower-dimensional perovskite QW photovoltaics to achieve higher efficiencies while maintaining stability. The hysteresis that is present in both the MA-only and mixed cation films needs to be addressed but can be overcome with strategies such as increasing ⟨n⟩[8] or preheating substrates prior to film deposition (hot-casting).[10]

CONCLUSION

This work illustrates that the choice of organic ligand can be exploited to influence beneficially the distribution in QW widths in low-dimensional perovskites. This control can in turn be used to improve the materials' optoelectronic properties. Within a polydisperse distribution, lower-dimensional QWs can act as ultrafast shallow traps for holes in materials with intermediately high ⟨n⟩. This severely limits hole diffusion lengths, while the nonflat energy landscape similarly slows electron mobility. Materials using the ligand allylammonium (ALA) result in a greatly reduced number of lower-n QWs, and therefore a reduced number of hole traps. Photovoltaics based on ALA perovskite QWs exhibit better efficiency while maintaining stability, indicating that controlling the QW width distribution is crucial to overcoming the performance−stability compromise in low-dimensional perovskite devices.

EXPERIMENTAL SECTION

Synthesis of Allylammonium Iodide. A typical reaction entailed mixing 7.5 mL of allylamine (5.7 g, 0.1 mol) into 15−30 mL of isopropanol (IPA) cooled in an ice bath. A cold (~4 °C, stored in a fridge prior) solution of 12.3 mL of 57% HI (0.9 mol of HI) is added dropwise to the cooled allylamine/IPA mixture. This mixture is left to react for 2 h, slowly warming up to room temperature (e.g., allow ice to melt in bath instead of replacing). The solvent is then evaporated under reduced pressure, and the remaining white solid is left to dry for an additional 30 min under mild heating and vacuum (the temperature was maintained at 70 °C max to evaporate any water from the HI solution). The solid is then stirred in diethyl ether for 10−15 min before being filtered and washed five times with more diethyl ether. This washed solid white powder is then recrystallized by dissolving it in boiling IPA and subsequently reprecipitating with diethyl ether. The recrystallized solid is isolated via vacuum filtration, washed an additional three times with diethyl ether, and then held under a vacuum for 16 h before being brought into a nitrogen glovebox for storage and use.

Preparation of Perovskite Precursor Solutions. Precursor solutions were prepared by dissolving mixtures of lead(II) iodide (PbI_2), lead(II) bromide ($PbBr_2$), methylammonium iodide (MAI), methylammonium bromide (MABr), formadinium iodide (FAI), cesium iodide (CsI), phenethylammonium iodide (PEAI), butylammonium iodide (BTAI), and allylammonium iodide (ALAI) in the solvents DMF, DMSO, or GBL. For the only MA, only I ⟨n⟩ = 10 films, we use the formula $ALA_2MA_9Pb_{10}I_{29}$, with $[Pb^{2+}]$ = 1.4−1.6 M in a 1:1 mixture of DMSO:GBL. This solvent mixture is used throughout the manuscript unless otherwise stated, and ALA is always interchangeable with PEA or BTA. For the mixed cation, mixed halide ⟨n⟩ = 10 films, we use the formula $ALA_2(MA_{0.14}FA_{0.81}Cs_{0.05})_9Pb_{10}(I_{0.85}Br_{0.15})_{29}$, with $[Pb^{2+}]$ = 1.4−1.6 M, and for the mixed cation, only I ⟨n⟩ = 10 films, we use the formula $ALA_2(MA_{0.14}FA_{0.81}Cs_{0.05})_9Pb_{10}I_{29}$.

Example of a typical preparation of a 0.5 mL, $[Pb^{2+}]$ = 1.6 M precursor solution: In a nitrogen glovebox, 368.8 mg (0.80 mmol) of PbI_2, 16.3 mg (0.103 mmol) of MAI, 100 mg (0.58 mmol) of FAI, 9.4 mg (0.04 mmol) of CsI, and 29.6 mg (0.16 mmol) of ALAI are dissolved in 0.5 mL of a 1:1 mixture of GBL:DMSO. This solution is heated to 70 °C and stirred at this temperature for at least 1 h before being cooled to room temperature, and filtered (0.22 μm, PTFE) into a new vial to be suitable for deposition.

Deposition of Perovskite Films. A 70−80 μL portion of perovskite precursor solution was dropped onto a substrate for a two-step spinning procedure. The first step was 1000 rpm for 10 s with an acceleration of 100 rpm s^{-1}, followed by 5000 rpm for 60 s with an acceleration of 800 rpm s^{-1}. 100 μL of chlorobenzene antisolvent is dropped onto the spinning substrate 30 s into the second spinning

DOI: 10.1021/jacs.7b12551
J. Am. Chem. Soc. XXXX, XXX, XXX−XXX

step. The substrate is then transferred onto a hot plate at 100 °C to be annealed for 30 min. This procedure is identical for depositing films on glass and on substrates for device fabrication. For films on glass, the substrates are first treated with oxygen plasma for 5 min before spin-coating the perovskite.

Photoluminescence Measurements. PL measurements were performed using a Horiba Fluorolog Time Correlated Single Photon Counting (TCSPC) system with photomultiplier tube detectors. A pulsed laser diode (507 nm, 110−140 ps pulse width) was used as the excitation source for steady-state and transient measurements. For transient and steady-state measurements, a 200 ns period (0.28 nJ per pulse) was used to capture accurate carrier lifetimes.

Photoluminescence Quenching Experiments. Films are prepared with identical precursor stoichiometry, but the solutions are diluted to $[Pb^{2+}]$ = 0.85 M in order to obtain thinner (∼200 nm) films. In a nitrogen glovebox, perovskite films are deposited onto glass substrates and annealed following the method described above. After the films have cooled, the quenching layers are deposited using the same spin-coating parameters and solution concentrations as Stranks et al. 20: solutions (in chlorobenzene) of PMMA (10 mg/mL), PCBM (30 mg/mL), and spiro-OMeTAD (65 mg/mL) are prepared. The PMMA and PCBM solutions are spin-coated at 1000 rpm for 20 s, and the spiro-OMeTAD film is spin-coated at 2000 rpm for 20 s.

Transient Absorption Measurements. Femtosecond laser pulses of a 1030 nm fundamental beam at a 5 kHz repetition rate were produced using a regeneratively amplified Yb:KGW laser (PHAROS, Light Conversion). Part of the fundamental beam was used to pump an optical parametric amplifier (ORPHEUS, Light Conversion) to serve as a narrowband pump with a tunable wavelength of 320−2200 nm (the pump wavelengths used in this study were 400, 610, and 640 nm), while the other part was focused into a sapphire crystal to generate a white-light supercontinuum probe (400−800 nm window). Both the pump and probe pulses were directed into a commercial transient absorption spectrometer (Helios, Ultrafast). Delaying the probe pulse relative to the pump provides a time window of up to 8 ns, and the time resolution of these experiments was ∼300 fs (estimated by the rise time of signal amplitudes in transient absorption spectra). All measurements were performed using an average power of 20 μW (for all wavelengths) with a spot size of ∼0.40 μm^2, assuming a Gaussian beam profile.

Device Fabrication. Prepatterned indium tin oxide (ITO, TFD Devices) coated glass substrates were sonicated in acetone and isopropanol sequentially for 30 min each before being dried under a flow of nitrogen gas. Titanium oxide (TiO_2) nanoparticles prepared according to ref 25 were deposited at 3000 rpm for 30 s with no ramping; this step is repeated twice. The substrates are then annealed at 150 °C for 30 min in air, cooled, and then brought into a nitrogen glovebox. The perovskite layer is deposited as described above. After the perovskite layer is annealed and cooled, a solution of spiro-OMeTad (65 mg/mL), doped with 20 μL/mL of *tert*-butylpyridine and 70 μL/mL of bis(trifluoromethane)sulfonimide lithium salt (170 mg/mL in acetonitrile), is deposited by spinning at 4000 rpm for 20 s with an acceleration of 2000 rpm s^{-1}. A 120 nm Au contact is deposited by electron-beam evaporation at a rate of 1.0 Å s^{-1}.

Device Testing. The current density−voltage (J−V) characteristics were measured using a Keithley 2400 source meter under the illumination of the solar simulator (Newport, Class A) at a light intensity of 100 mW cm^{-2} as checked with a calibrated reference solar cell (Newport). Unless otherwise stated, the J−V curves were all measured in a nitrogen atmosphere with a scanning rate of 50 mV s^{-1} (voltage step of 10 mV and delay time of 200 ms). The active area was determined by the aperture shade mask (0.049 cm^2 for small-area devices) placed in front of the solar cell. A spectral mismatch factor of 1 was used for all J−V measurements. The dark long-term stability assessment of solar cells was carried out by repeating the J−V characterizations over various times (∼1 week apart each). The devices were stored in a cabinet with dry air with a relative humidity between 30 and 40%. The chamber containing the cells for testing was purged with and maintained under nitrogen flow during the measurements.

Grazing-Incidence Wide-Angle X-Ray Scattering (GIWAXS). GIWAXS data was collected at the National Synchrotron Radiation Research Center in Hsinchu, Taiwan. Two-dimensional scattering was collected at a 2° incidence, with monochromatic 15 keV X-Rays and recorded on a flat panel detector measuring 50 × 50 mm^2. Samples were measured in air. Data for phenethylammonium samples was collected at the Stanford Synchrotron Radiation Lightsource at a 2° incidence, monochromatic 12.7 keV X-Rays, and recorded on a Rayonix Mx-225 detector measuring 225 × 225 mm^2. Samples were measured in a chamber filled with helium. All images were calibrated using LaB6 and integrated to 1D patterns using the Nika software package[28] and the GIXSGUI MATLAB plugin.[29]

■ ASSOCIATED CONTENT

Supporting Information

The Supporting Information is available free of charge on the ACS Publications website at DOI: 10.1021/jacs.7b12551.

Materials and methods and supplementary Figures S1−S16 (PDF)

■ AUTHOR INFORMATION

Corresponding Author

*ted.sargent@utoronto.ca

ORCID

Andrew H. Proppe: 0000-0003-3860-9949
Rafael Quintero-Bermudez: 0000-0002-4233-395X
Oleksandr Voznyy: 0000-0002-8656-5074
Shana O. Kelley: 0000-0003-3360-5359

Notes

The authors declare no competing financial interest.

■ ACKNOWLEDGMENTS

This publication is based in part on work supported by an award (N00014-17-1-2524) from the Office of Naval Research (ONR), by the Ontario Research Fund Research Excellence Program, and by the Natural Sciences and Engineering Research Council (NSERC) of Canada (Discovery Grant 2016-06090). A.H.P. acknowledges support from the Ontario Graduate Scholarship (OGS) program. H.T. acknowledges The Netherlands Organization for Scientific Research (NWO) for a Rubicon grant (680-50-1511) in support of his postdoctoral research at the University of Toronto. We thank Mike Toney and Aryeh Gold-Parker at the Stanford Synchrotron Radiation Lightsource and U-Ser Jeong at the National Synchrotron Radiation Research Center for assistance with GIWAXS measurements.

■ REFERENCES

(1) Dong, Q.; Fang, Y.; Shao, Y.; Mulligan, P.; Qiu, J.; Cao, L.; Huang, J. *Science* **2015**, *347*, 967.

(2) Xing, G.; Mathews, N.; Sun, S.; Lim, S. S.; Lam, Y. M.; Grätzel, M.; Mhaisalkar, S.; Sum, T. C. *Science* **2013**, *342*, 344.

(3) Shi, D.; Adinolfi, V.; Comin, R.; Yuan, M.; Alarousu, E.; Buin, A.; Chen, Y.; Hoogland, S.; Rothenberger, A.; Katsiev, K.; Losovyj, Y.; Zhang, X.; Dowben, P. A.; Mohammed, O. F.; Sargent, E. H.; Bakr, O. M. *Science* **2015**, *347*, 519.

(4) Yang, W. S.; Park, B.-W.; Jung, E. H.; Jeon, N. J.; Kim, Y. C.; Lee, D. U.; Shin, S. S.; Seo, J.; Kim, E. K.; Noh, J. H.; Seok, S. I. *Science* **2017**, *356*, 1376.

(5) Weidman, M. C.; Seitz, M.; Stranks, S. D.; Tisdale, W. A. *ACS Nano* **2016**, *10*, 7830.

(6) Wang, Z.; Lin, Q.; Chmiel, F. P.; Sakai, N.; Herz, L. M.; Snaith, H. J. *Nat. Energy* **2017**, *2*, 17135.

DOI: 10.1021/jacs.7b12551
J. Am. Chem. Soc. XXXX, XXX, XXX−XXX

(7) Byun, J.; Cho, H.; Wolf, C.; Jang, M.; Sadhanala, A.; Friend, R. H.; Yang, H.; Lee, T.-W. *Adv. Mater.* **2016**, *28*, 7515.
(8) Quan, L. N.; Yuan, M.; Comin, R.; Voznyy, O.; Beauregard, E. M.; Hoogland, S.; Buin, A.; Kirmani, A. R.; Zhao, K.; Amassian, A.; Kim, D. H.; Sargent, E. H. *J. Am. Chem. Soc.* **2016**, *138*, 2649.
(9) Zhang, X.; Ren, X.; Liu, B.; Munir, R.; Zhu, X.; Yang, D.; Li, J.; Liu, Y.; Smilgies, D.-M.; Li, R.; Yang, Z.; Niu, T.; Wang, X.; Amassian, A.; Zhao, K.; Liu, S. *Energy Environ. Sci.* **2017**, *10*, 2095.
(10) Tsai, H.; Nie, W.; Blancon, J.-C.; Stoumpos, C. C.; Asadpour, R.; Harutyunyan, B.; Neukirch, A. J.; Verduzco, R.; Crochet, J. J.; Tretiak, S.; Pedesseau, L.; Even, J.; Alam, M. A.; Gupta, G.; Lou, J.; Ajayan, P. M.; Bedzyk, M. J.; Kanatzidis, M. G.; Mohite, A. D. *Nature* **2016**, *536*, 312.
(11) Cao, D. H.; Stoumpos, C. C.; Farha, O. K.; Hupp, J. T.; Kanatzidis, M. G. *J. Am. Chem. Soc.* **2015**, *137*, 7843.
(12) Xiao, Z.; Kerner, R. A.; Zhao, L.; Tran, N. L.; Lee, K. M.; Koh, T.-W.; Scholes, G. D.; Rand, B. P. *Nat. Photonics* **2017**, *11*, 108.
(13) Kim, H.; Lim, K.-G.; Lee, T.-W. *Energy Environ. Sci.* **2016**, *9*, 12.
(14) Wang, Z.; Lin, Q.; Chmiel, F. P.; Sakai, N.; Herz, L. M.; Snaith, H. J. *Nature Energy* **2017**, *2*, 17135.
(15) Yuan, M.; Quan, L. N.; Comin, R.; Walters, G.; Sabatini, R.; Voznyy, O.; Hoogland, S.; Zhao, Y.; Beauregard, E. M.; Kanjanaboos, P.; Lu, Z.; Kim, D. H.; Sargent, E. H. *Nat. Nanotechnol.* **2016**, *11*, 872.
(16) Liu, J.; Leng, J.; Wu, K.; Zhang, J.; Jin, S. *J. Am. Chem. Soc.* **2017**, *139*, 1432.
(17) Shang, Q.; Wang, Y.; Zhong, Y.; Mi, Y.; Qin, L.; Zhao, Y.; Qiu, X.; Liu, X.; Zhang, Q. *J. Phys. Chem. Lett.* **2017**, *8*, 4431.
(18) Wu, X.; Trinh, M. T.; Zhu, X.-Y. *J. Phys. Chem. C* **2015**, *119*, 14714.
(19) Snellenburg, J. J.; Laptenok, S. P.; Seger, R.; Mullen, K. M.; van Stokkum, I. H. M. *J. Stat. Soft.* **2012**, *49*, 1.
(20) Stranks, S. D.; Eperon, G. E.; Grancini, G.; Menelaou, C.; Alcocer, M. J. P.; Leijtens, T.; Herz, L. M.; Petrozza, A.; Snaith, H. J. *Science* **2013**, *342*, 341.
(21) Lee, E. M. Y.; Tisdale, W. A. *J. Phys. Chem. C* **2015**, *119*, 9005.
(22) Liu, M.; Voznyy, O.; Sabatini, R.; Garcia de Arquer, F. P.; Munir, R.; Balawi, A. H.; Lan, X.; Fan, F.; Walters, G.; Kirmani, A. R.; Hoogland, S.; Laquai, F.; Amassian, A.; Sargent, E. H. *Nat. Mater.* **2017**, *16*, 258.
(23) Zhitomirsky, D.; Kramer, I. J.; Labelle, A. J.; Fischer, A.; Debnath, R.; Pan, J.; Bakr, O. M.; Sargent, E. H. *Nano Lett.* **2012**, *12*, 1007.
(24) Soe, C. M. M.; Stoumpos, C. C.; Kepenekian, M.; Traoré, B.; Tsai, H.; Nie, W.; Wang, B.; Katan, C.; Seshadri, R.; Mohite, A. D.; Even, J.; Marks, T. J.; Kanatzidis, M. G. *J. Am. Chem. Soc.* **2017**, *139*, 16297.
(25) Tan, H.; Jain, A.; Voznyy, O.; Lan, X.; García de Arquer, F. P.; Fan, J. Z.; Quintero-Bermudez, R.; Yuan, M.; Zhang, B.; Zhao, Y.; Fan, F.; Li, P.; Quan, L. N.; Zhao, Y.; Lu, Z.-H.; Yang, Z.; Hoogland, S.; Sargent, E. H. *Science* **2017**, *355*, 722.
(26) Jeon, N. J.; Noh, J. H.; Yang, W. S.; Kim, Y. C.; Ryu, S.; Seo, J.; Seok, S. I. *Nature* **2015**, *517*, 476.
(27) McMeekin, D. P.; Sadoughi, G.; Rehman, W.; Eperon, G. E.; Saliba, M.; Hörantner, M. T.; Haghighirad, A.; Sakai, N.; Korte, L.; Rech, B.; Johnston, M. B.; Herz, L. M.; Snaith, H. J. *Science* **2016**, *351*, 151.
(28) Ilavsky, J. *J. Appl. Crystallogr.* **2012**, *45*, 324−328.
(29) Jiang, Z. *J. Appl. Crystallogr.* **2015**, *48*, 917−926.

DOI: 10.1021/jacs.7b12551
J. Am. Chem. Soc. XXXX, XXX, XXX−XXX